# Probing proton diffusion as a guide to environmental stability in powder-engineered FAPbI3 and CsFAPbI3 perovskites

Muhammed P.U. Haris, Jianxing Xia, Samrana Kazim, Zuzanna Molenda, Lionel Hirsch, Thierry Buffeteau, Dario M Bassani, Mohammad Khaja Nazeeruddin, Shahzada Ahmad

# Probing Proton Diffusion as a Guide to Environmental Stability in Powder-Engineered $FAPbI_3$ and $CsFAPbI_3$ Perovskites

Muhammed P. U. Haris[1], Jianxing Xia[2], Samrana Kazim[1,5], Zuzanna Molenda[3], Lionel Hirsch[3], Thierry Buffeteau[4], Dario M. Bassani[4], Mohammad Khaja Nazeeruddin[2], and Shahzada Ahmad[1,5,6]*

[1]BCMaterials, Basque Center for Materials, Applications, and Nanostructures, UPV/EHU Science Park, 48940, Leioa, Spain
Email: shahzada.ahmad@bcmaterials.net; shahzadaahmada@ehu.eus
[2]Group for Molecular Engineering of Functional Materials, Institute of Chemical Sciences and Engineering, École Polytechnique Fédérale de Lausanne, Valais Wallis, Rue de l'Industrie 17, 1950 Sion, Switzerland
[3]Univ. Bordeaux, CNRS, Bordeaux INP, ENSCBP, IMS, CNRS UMR 5218, F-33400 Talence, France
[4]Univ. Bordeaux, CNRS, Bordeaux INP, ISM, UMR 5255, F-33405, Talence, France
[5]IKERBASQUE, Basque Foundation for Science, Bilbao, 48009, Spain
[6]Lead contact
*Correspondence: shahzada.ahmad@bcmaterials.net; shahzadaahmada@ehu.eus

## SUMMARY

Pre-synthesized perovskite powder is advantageous for device reliability. Arguably, the water uptake capability is critical for the stability of α-$FAPbI_3$ thin films, and the migration of hydrogen species is challenging to elucidate using routine techniques such as imaging or mass spectroscopy. Here, we decipher the proton diffusion to quantify indirect monitoring of H migration by following the N–D vibration using transmission infrared spectroscopy. Allows the direct assessment of the deterioration of perovskite by moisture. The inclusion of a minor amount of Cs in $FAPbI_3$, reveals significant differences in proton diffusion rates attesting to its impact. Its ability to access the active layer by water molecules is five times, lower than $FAPbI_3$, which is lower than $MAPbI_3$. This protocol directly correlates with the local environment of the materials and engages with a range of semiconductors to identify the material's reliability and intrinsic degradation mechanisms toward its suitability for optoelectronic applications.

## INTRODUCTION

In the emerging solar cells category, a monumental research focus has been given to the field of perovskite solar cells (PSCs) in the last decade.[1] The first reported methylammonium lead triiodide ($MAPbI_3$) based PSCs showed competitive results, which was followed by compositional engineering of the perovskites to harvest more solar energy, in terms of higher photo-current and open-circuit voltage engineering through the materials composition variation.[2] However, the concern of volatility of methylammonium (MA) in the former, and phase segregation in the latter, led to the renaissance of formamidinium lead triiodide ($FAPbI_3$) for solar cell fabrication. [3–5] Among other merits, such as favorable lower bandgap for improved light harvesting, long-term thermal stability due to the higher activation energy for thermal degradation, and improved bulk stability due to the self-healing property of formamidinium ion,[6] their switching of photo-active (α-phase) to photo-inactive (δ-phase, yellow) phase compromises reliability issues under operational conditions.[7] The phase transition to the thermodynamically stable δ-phase is initiated through the lattice strain relaxation and further accelerated by diverse environmental forces.[8] To overcome such grievances, various strategies such as compositional,[9,10] additive,[11] dimensionalities,[12] passivation[13] and process engineering,[14-16] have been adopted by the research community, to deliver significant advancements in terms of power conversion efficiencies (PCE) and phase stability for $FAPbI_3$-based PSCs. The engineering of composition, in particular, the multi-cation combination (MA, $Cs^+$, and $Rb^+$ with FA) with different halide anions emerged as a path to fabricate efficient PSCs. Recent investigations at the localized level (nanostructure) revealed that the triple cation perovskites show a tilted octahedral formation which boosted the phase stability. However, further studies suggested that phase stability is restricted only to the macroscopic level and the inhomogeneously-tilted octahedra accelerate the phase segregation followed by the creation of deep traps and photo-generation pathways.[17] Owing to the substantial advancement made in $MAPbI_3$ based PSCs, rational choice of additives and passivation successfully addressed the phase instability issue, and the PCE skyrocketed through

strain engineering. Methylene diammonium dichloride has been introduced as an additive and their employment along with smaller $Cs^+$ mitigated the lattice strain and achieved higher efficiency of 24.4% and the PSCs maintained >80% of their initial PCE after 1300 h in the dark at 85 °C.[18]

In addition to the high PCEs, reliability is critical for PSCs to enter the commercialization endeavor of PSCs, while the PV market relies broadly on operational costs. Moisture or humidity is the main factor for degradation while other environmental scenarios such as heat, light, and combinations of factors alleviate this.[19-23] Moisture-induced degradation accelerates intrinsic instability. With the herald, building abound $FAPbI_3$ as a material of choice, a direct, rapid, and reliable approach is paramount to investigating and developing fast and efficient screening of materials. Water ingress into the perovskite layer may proceed through i) mono-, di-hydrate formations, ii) strong water-organic amine interaction induced degradation through the weakening of cation-$PbI_6$ interaction, and iii) protonation of iodide to form hydroiodic acid leaving $PbI_2$ behind as the final decomposition product.[19] Understanding the reaction kinetics and mechanistic origin are pivotal to designing robust perovskite-based absorbers. Ion diffusion into the perovskite grains occurred as a result of ion migration at grain boundaries and in the bulk, this negatively affects the overall device performance.[24,25] Quantifying experimental approaches to monitor water uptake will be beneficial, although current techniques such as TOF-SIMS[26] do not apply to hydrogen species ($H^+$, $H^0$, and $H^{-1}$), it can be studied by neutron scattering experiments.[27] However, this requires access to large-scale radiation facilities and planning. The development of experimental techniques for tracking the migration of hydrogen species is of significance to deciphering the stability of designed materials. One such technique is polarization-modulated infrared reflection–absorption spectroscopy (PM-IRRAS),[28] which can track the migration of hydrogen species in $MAPbI_3$ by registering the difference in the vibrational frequency of X–H vs X–D bonds during isotope exchange processes, where X is a heavier element such as carbon, oxygen, or nitrogen.[28] Alternatively, the H / D

composition of the material can also be determined using NMR spectroscopy after the dissolution of the material.[29]

As an extension of this work, we employ transmission infrared (IR) spectroscopy using a sealed cell to follow the isotope exchange under controlled conditions. We show that this is a particularly suitable technique as it allows direct probing of local environmental effects, such as relative humidity, on the migration of hydrogen species. Additionally, we have opted for powder-engineered perovskites as the choice of material owing to i) achieving the highest PCEs and reproducibility over their conventional counterpart,[30-32] ii) reduction in the microstrain and Urbach energy values for perovskite layers fabricated from the powder engineering process, indicating mitigated structural and electronic disorders.[32] Additionally, the powder methodology, would overcome the Pb impurities issue from the Pb precursors and elimnate the error in the weighing of the precursors. The indirect assessment of the protection against moisture induced by surface modification of the powder-engineered α-$FAPbI_3$ and α-$CsFAPbI_3$ can be obtained by simply monitoring the rate of hydrogen exchange within the active layer in the presence of ambient moisture. This knowledge can be used to predict the material´s propensity towards moisture-induced defect formation. Optimization of such process and materials design rule will suppress the non-radiative recombination of photo-generated charge carriers, paving way for higher fill factor and the $V_{OC}$ in PSCs. With this in hand, we further improve the performance of powder-engineered PSCs with promising fluorinated ionic liquids as an additive.

## RESULTS AND DISCUSSION

### Preparation and characterization of thin films

Hereafter we use the term ˙$FAPbI_3$ from δ-powder' and ˙$FAPbI_3$ from α-powder' for $FAPbI_3$ thin films fabricated from the pre-synthesized δ-phase and α-phase powders respectively. The synthesis

of δ-phase and α-phase powders are detailed in the experimental section, briefly δ-phase powder was precipitated by stirring lead iodide ($PbI_2$) with the formamidinium iodide containing acetonitrile solution at room temperature. The α-$FAPbI_3$ powder was realized by annealing the δ-phase powder at 150 °C. Thin films of the perovskites were prepared by spin-coating precursor solutions onto a 2 mm thick $BaF_2$ disk (20 mm diameter). Upon annealing to 150 °C for 30 min, both $FAPbI_3$, ie $FAPbI_3$ from δ-, and α–powders, gave dark brown films with identical UV-vis spectra. Scanning probe microscopy (SPM) images (Fig. S1) were collected on each sample to determine grain size.

**Proton diffusion studies**

The samples were placed in a home-built spectroscopic cell that hermetically seals the $BaF_2$ substrate inside a controlled environment. After measuring the transmission IR spectrum at $t$ = 0, a saturated solution of $K_2CO_3$ in $D_2O$ is injected into the cell to maintain the relative humidity fixed at 43%. Successive IR spectra are then taken to determine the proportion of H / D exchange taking place in the material over time.

The spectral variation during the H / D exchange for the $FAPbI_3$ from the α-powder sample is shown in Figure 1A in the 1850-1250 $cm^{-1}$ region. At t=0, the IR spectrum exhibits three main bands at 1712, 1613, and 1352 $cm^{-1}$, with strong, weak, and medium intensities, respectively. The 1712 and 1352 $cm^{-1}$ bands are coupled modes involving νCN, $\delta NH_2$, and δCH vibrations; the 1712 $cm^{-1}$ mode is dominated by the νCN (50%) and $\delta NH_2$ (40%) components whereas the 1352 $cm^{-1}$ mode is dominated by the δCH (72%) component. The 1613 $cm^{-1}$ mode is pure $\delta NH_2$ vibration.[33] Upon $D_2O$ exposition, the 1712 and 1352 $cm^{-1}$ bands decreased in favor of the increase of the 1681 and 1336 $cm^{-1}$ bands, respectively, whereas the decrease of the $\delta NH_2$ band at 1613 $cm^{-1}$ mode is associated with the increase of the $\delta ND_2$ band at 1393 $cm^{-1}$ (Figure 1A). It is important to note that only the H in the $NH_2$ fragment will exchange with $D_2O$. The H / D exchange for the α-$FAPbI_3$ sample can be

followed by either the spectral variation of the pure $\delta NH_2$ mode or by the sum of the spectral variation of the two bands related to the coupled modes involving νCN, $\delta NH_2$, and δCH vibrations. Both were found to give identical kinetic profiles but, due to the weaker intensity of the $\delta NH_2$ mode, the spectral vibration of the coupled modes of νCN and δCH were selected.

The variations in the spectral data are related to the exchange of the labile N–H protons in $FAPbI_3$ by deuterium, which causes a shift of the vibration to lower frequencies due to its higher mass. This is a complex process that we can decompose into 3 steps: (i) dissociation of $D_2O$ on the surface of the substrate, (ii) diffusion of $D^+$ into the sample, and (iii) H / D substitution in the formamidinium cation. Both the dissociation of $D_2O$ and isotopic substitution are expected to be fast with respect to ion diffusion in the solid, which should therefore be rate-limiting. The diffusion of a species in a solid follows Fink's law stating that the rate of diffusion of a species is proportional to the concentration gradient of that species. The exact solutions of Fink's law depend on the experimental conditions. For the diffusion in nano-crystalline perovskite thin films, we have evidenced that high-diffusivity pathways between grains are important in determining the diffusion rate. Indeed, the measured diffusion rates are relatively insensitive to sample thickness in agreement with a model in which diffusion occurs rapidly around the grains, and more slowly inside.[34] The individual grains can be modeled as spheres of radius R, and the bulk sample's H / D exchange is obtained by integrating over the thickness of the sample (eq 1):

$$m(t) = \frac{M}{M_{total}} = 1 - \frac{6}{\pi^2}\sum_{n=1}^{\infty}\frac{1}{n^2}e^{-D\frac{n^2\pi^2}{R^2}t} \quad (1)$$

Where $m(t)$ is the fraction of total deuterium present at time $t$, $M$ is the intensity of the signal for the deuterated species present, $D$ is the diffusion constant, and $R$ is the radius of the sphere approximating the grain size or lattice domain.

As mentioned above, the vibrations of the N–H(D) and C–H are strongly coupled. Because of this, it is not possible to individually discriminate between the partially deuterated species as is the case for $MAPbI_3$, where the sequential transformation of $CH_3NH_3^+ \rightarrow CH_3NH_2D^+ \rightarrow CH_3NHD_2^+ \rightarrow CH_3ND_3^+$ can be resolved. Furthermore, the contribution of the C–H vibrators (which do not undergo isotope exchange) should be deducted from the overall signals to obtain exclusively the changes resulting from the N–H to N–D exchange. To simplify this, we identified the vibration at vibrations at 1712 $cm^{-1}$, 1681 $cm^{-1}$, 1352 $cm^{-1}$, and 1336 cm–1 to be exclusively (or nearly so) due to N–H / D vibrators. For these bands, the loss of the N–H contribution (at 1712 $cm^{-1}$ and 1352 $cm^{-1}$) is fully compensated by the grow-in of the N–D species (at 1681 $cm^{-1}$ and 1336 $cm^{-1}$) as shown in Figure 1B, C) as shown in Figure 2A. From this, it is possible to verify that the loss of H can be precisely quantified from the sum of the intensities of the vibrations at 1712 $cm^{-1}$ and 1352 $cm^{-1}$. The data may then be fitted to eq(1) using a value of *R* corresponding to the average grain size (Table 1) determined by SPM and surface SEM images for each sample (Figure S1).

The results for the analysis of the diffusion of $D^+$ into thin films of $FAPbI_3$ or $CsFAPbI_3$ exposed to $D_2O$ are summarized in Table 1. The diffusion constants were determined using the corresponding average grain size for each sample as derived from the analysis of the AFM and SEM images (Figure S1). Overall, the diffusion coefficients are smaller than that previously determined for $MAPbI_3$ ($D$ = $1.5 \times 10^{-15}$ $s.cm^{-2}$). As expected, $FAPbI_3$ films prepared from either α-powder or δ-powder gave nearly identical results, in agreement with the observation that the nature of the precursor material does not affect the properties of the post-annealed active layer. It can also be seen that the rate of diffusion of protons into $CsFAPbI_3$ from α-powder is only one-fifth that of $FAPbI_3$. Interestingly, the proton diffusion rate constants are greatest for $MAPbI_3$ and the smallest for $CsFAPbI_3$, with $MAPbI_3$ > $FAPbI_3$ > $CsFAPbI_3$. This is also the same order that is generally observed for the propensity towards damage by ambient moisture in halide perovskite materials, and we may speculate that the

propensity of lead halide perovskite materials towards damage by moisture is related to the proton diffusion rate for the material. A similar observation was earlier made from the comparison of MAPI active layers in the absence of different adlayers capable of reducing moisture degradation. In this case, the rate of isotope substitution was found to be slowest for those adlayers offering the greatest protection.[28] We also note that the fit of the experimental data for the $CsFAPbI_3$ from the α-powder sample shows some deviation from eq(1) which may reflect intra-grain inhomogeneity due to the partial substitution of FA by $Cs^+$.

Though reports appear to suggest a performance enhancement in powder-engineered $FAPbI_3$ PSCs,[14,30-32] the reason for intrinsic stability remains undiscovered to an extent. While comparing the conventional and powder engineering methods, we speculate that the precursor solution step acts as a Y-junction in the perovskite fabrication process and their investigations are crucial. It has been suggested that the perovskite precursor solution is a low-viscous solution that comprises polyiodide plumbates which drive the nucleation and crystallization upon further spin coating and annealing.[35] To unravel the different scenarios between conventional (c-$FAPbI_3$) and powder engineering (α-$FAPbI_3$) methods, we probed the corresponding $FAPbI_3$ precursor solutions using proton nuclear magnetic resonance spectroscopy. With the presence of $PbI_2$, the protons attached to two nitrogen atoms showed fast resonances which lead to the peak broadening (Figure 3). A slight peak broadening of -CH protons was also visible in the powder method than in the conventional counterpart. Arguably, such observations are attributed to the difference in the local protonic environment in the precursor solution which in turn impacts the photo-physical properties of the corresponding perovskite thin films.

**Fabrication and analysis of PSCs**

The photovoltaic performances of the PSCs employing $FAPbI_3$ and $CsFAPbI_3$ from α-powders were probed in an FTO/c-$TiO_2$/m-$TiO_2$/$SnO_2$/Perovskite/Spiro-OMeTAD/Au device structure (Figure 4A). Expectedly,[36,37] the $CsFAPbI_3$ based PSCs exhibit a higher PCE of 19.2% as compared to 18.8% for $FAPbI_3$ based PSCs, and the steady-state efficiency of 19.14% (Figure 4B, C) is measured for $CsFAPbI_3$.

To suppress the inhibition of ionic migration and a further improvement in the performance of PSCs, we adopted doping by ionic liquids, this will also reduce the ionic migration within the $CsFAPbI_3$ perovskite thin-film. We employed, the 1,3-bis(cyanomethyl)imidazolium bis(trifluoromethylsulfonyl)imide (IL)[38] as an additive into perovskite. The ionic liquid additivisation improved the crystallization of the perovskite layer and yielded an improvement in the thickness from 530 nm to 580 nm (Figure S2) as a result of the controlled crystallization process. The improved crystallization of perovskite film may attribute to the changing of surface tension within the precursor and the coordination between ionic liquid and $PbI_2$.[39,40] Figure 4D exhibits the *J-V* curves of PSCs based on various concentrations of IL doping. At the doping concentration of 0.7 mol%, the PCE of the PSCs improved to 20.55% (Table 2, Figure S3), while under similar conditions the reference $CsFAPbI_3$-based PSCs measured 19.27% in the same batch. The steady-state efficiency of the devices was compared (Figure 4E), and the PSC doped with IL displayed 20.38% PCE after 130 s of continuous illumination, further we noted that the PCE is close to the value derived from the *J-V* curve, and under the similar condition the $CsFAPbI_3$ based PSCs measured a PCE of 19.13%. Furthermore, the integrated current density ($J_{SC}$) from the incident photon to current efficiency (IPCE) (Figure 4F) over the spectral range from 350 to 900 nm to measure the veracity of the $J_{SC}$ of the *J-V* curves. The integrated $J_{SC}$ of PSCs based on references and doped with IL respectively achieved 22.86 and 22.81 mA $cm^{-2}$ which is close to the short-circuit current density

($J_{SC}$) value from the *J-V* curves with a slight loss of 7%. We attribute these slight variations to the difference in the light source of *J-V* and IPCE used.

We performed the Time-Resolved Photoluminescence (TRPL) measurements (Figure 4G) of pristine and IL-doped $CsFAPbI_3$ on a structure of glass/perovskite to deduce the carrier lifetime of perovskite film, as well as the decay times. The data are fitted by a *mono*-exponential model at a long decay regime with $\tau$ components which indicated recombination.[41] On the additivisation of $CsFAPbI_3$ film with IL, the decay time ($\tau$) of TRPL increased from 516.1 to 614 ns indicating the reduced recombination of photogenerated electrons and hole, which is attributed to the passivation of trap states by the ionic liquid.[38]

To conclude, here we employed transmission IR spectroscopy and demonstrated the suitability in allowing the tracking of local environment scenarios against the humidity and made quantification of ion migration to unravel the material´s intrinsic properties for device improvement. We noted the proton diffusion rate constants follow the order of $MAPbI_3$ > $FAPbI_3$ > $CsFAPbI_3$, and are lowest for $CsFAPbI_3$. The majority of techniques fall short to probe hydrogen species migration, our report reveals guidelines for deciphering the $H^+$ migration and diffusion coefficient to increase the photo-stability of perovskites. The incorporation of Cs not only pushes the performance but also significantly reduces the diffusion coefficient by five times in $FAPbI_3$. The development of such a protocol is an effective and rapid means to screen the viability of the material for perovskite solar cells technology and assess the fundamental limit of the materials to understand the local environment for reliability in a range of emerging semiconductors. We modeled the rate of H/D exchange employing first-order kinetics to elucidate numerical parameters that can be directly correlated to probe the effectiveness of surface modification on environmental exposure.

## Experimental procedures

## Resource availability

### *Lead contact*

Further information and requests for resources and reagents should be directed to and will be fulfilled by the lead contact, Shahzada Ahmad (shahzada.ahamad@bcmaterials.net).

### *Materials availability*

This study did not generate new unique materials.

### *Data and code availability*

This study did not generate datasets.

### Chemical materials

Titanium diisopropoxide bis(acetylacetonate) (TAA), 4-*tert*-butylpyridine (tbp), tin(IV) chloride pentahydrate, bis(trifluoromethane) sulfonamide lithium salt, and [tris(2-(1*H*-pyrazol-1-yl)-4-*tert*-butylpyridine)-cobalt(III) tris(bis(trifluoromethylsulfonyl)imide)] (FK209), chlorobenzene (CB), dimethylsulphoxide (DMSO), dimethylformamide (DMF), methylammonium hydrochloride (MACl) were supplied from Sigma-Aldrich. lead iodide ($PbI_2$) and cesium iodide (CsI) was purchased from TCI. 2,2′,7,7′-Tetrakis(*N*, *N*-di-4-methoxyphenylamine)-9,9′-spirobifluorene (spiro-OMeTAD) was purchased from Merck. 30-NRT was purchased from GreatCell. All of the purchased chemicals were used as received without further purification.

### Synthesis of $FAPbI_3$ δ-phase powder

The δ-phase powder was synthesized by using the room temperature precipitation method. The 10.7 mmol FAI (synthesized from formamidine acetate[1]) was dissolved in 100 ml of acetonitrile (HPLC grade, Alfa Aesar) by stirring, then 8.3 mmol of $PbI_2$ (99%) was added to the stirring solution and allowed the stirring to continue for 24 hours. The derived yellow powders were filtered and washed thoroughly (5-6 times) with acetonitrile and finally with diethyl ether to remove any residual $PbI_2$ and FAI. The yellow product was then dried under a continuous vacuum for another 24 hours and kept in the glove box until further use.

**Synthesis of $FAPbI_3$ α-phase powder**

The δ-phase powder was annealed in a tube furnace at 150 °C for 1 hour in an inert atmosphere to obtain a black α-phase powder. This black powder was kept in the glove box for further use.

**Synthesis of $CsFAPbI_3$ α-phase powder**

Acetonitrile solution containing CsI and FAI in a 1:9 ratio was used in this case and the rest procedure is the same as the above for $FAPbI_3$ α-phase powder

**Film and device fabrication**

The chemically etched FTO glass was cleaned with a detergent solution, acetone, and ethanol. For the compact $TiO_2$ (C-$TiO_2$) layer, TAA solution in ethanol (0.2 mL of TAA in 6 mL of anhydrous ethanol) was sprayed at 450 °C and heated for 1 h. The mesoporous $TiO_2$ (m-$TiO_2$, 30-NRT) was diluted at ethanol with a ratio of 1:10 and coated on the C-$TiO_2$ substrate at a speed of 3000 rpm for 20 s with a ramp-up of 2000 rpm $s^{-1}$ finally heating at 500 ℃ for 60 min. The $SnCl_4$ layer was dissolved in deionized water at a concentration of 12 μL/mL and spin-coating on the m-$TiO_2$ layer at a speed of 3000 rpm for 20 s with a ramp-up of 2000 rpm $s^{-1}$ finally heating at 190 ℃ for 60 min, and then perovskite solutions were formulated by dissolving 1.4 M α-$FAPbI_3$ or $CsFAPbI_3$ powder in DMSO/DMF mixed solvent with a ratio of 1:8, 20 mg MACl was also added to the perovskite solution. In the additivated perovskites, the ionic liquid was added in varying concentrations of IL into the perovskite precursors. All the perovskite solutions were filtered through a PTFE filter with a 450 nm pore size. The perovskite layers are fabricated by spin-coating at 1000 rpm for 10 s and 5000 rpm for 30 s, respectively. Then, 200 μL of chlorobenzene was dropped in 10 s at 5000 rpm. Perovskite films were annealed at 150 °C for 15 min. The HTM solution was prepared by dissolving 75 mg of Spiro-OMeTAD (Merck) with additives in 1 mL of chlorobenzene and film fabricated by spin-coating at 4000 rpm for 30 s. As additives, 18 μL of Li-bis(trifluoromethanesulfonyl) imide from the stock solution (520 mg in 1 mL of acetonitrile), 13 μL of FK209 [tris(2-(1*H*-pyrazol-1-yl)-

4-*tert*-butylpyridine)-cobalt(III) tris(bis (trifluoromethylsulfonyl)imide) (375 mg in 1 mL of acetonitrile), and 30 µL of 4-*tert*-butylpyridine were added. Finally, the deposition of the 70 nm thick Au electrode by thermal evaporation on the Spiro-OMeTAD.

**Material and thin-film characterizations**

For the TRPL measurements, samples were excited with a 408-nm pulsed laser (MDL 300, PicoQuant) with 40 µm·cm$^{-2}$ pulse energy density (pulse width 180 ps). $^{1}$H-NMR spectra were recorded using a Varian Mercury 400 MHz spectrometer in DMSO- d6 solvent at 25 °C. The cross-sectional and surface SEM images were acquired from a Hitachi S-4800 SEM machine. SPM images were acquired with the help of Autoprobe CP-Research microscope (VEECO) after the IR experiments. Transmission IR experiments were performed on a ThermoNicolet Nexus 670 FTIR spectrometer at a resolution of 4 cm$^{-1}$.

**Device characterizations**

Current-voltage characteristics were recorded by applying an external potential bias to the cell while recording the generated photocurrent with a digital source meter (Keithley Model 2400). The light source was a 450 W xenon lamp (Oriel) equipped with a SchottK113 Tempax sunlight filter (Praezisions Glas & Optik GmbH) to match the emission spectrum of the lamp to the AM 1.5G standard. Before each measurement, the exact light intensity was determined using a calibrated Si reference diode equipped with an infrared cutoff filter (KG-3, Schott). The cells were masked with the active area of 0.09 cm$^2$ to fix the active area and reduce the influence of the scattered light on the small device. IPCE spectra were recorded as functions of wavelength under a constant white light bias of ≈10 mW·cm$^{-2}$ supplied by an array of white light emitting diodes. The excitation beam coming from a 300 W xenon lamp (ILC Technology) was focused through a Gemini-180 double monochromator (Jobin Yvon Ltd) and chopped at ≈2 Hz. The signal was recorded using a Model SR830 DSP Lock-In Amplifier (Stanford Research Systems).

## SUPPLEMENTAL INFORMATION

Document S1. AFM surface and SEM surface of perovskite films, and cross-sectional SEM images of devices. Device statistics.

Supplemental information can be found online at …


## ACKNOWLEDGMENTS

This work received funding from the European Union H2020 Programme under a European Research Council Consolidator grant [MOLEMAT, 726360]. Support from the Spanish Ministry of Science and Innovation (PID2019-111774RB-100/AEI/10.13039/501100011033 and INTERACTION {PID2021-129085OB-I00}) and the French ANR (ANR-18-CE05-0021) is also acknowledged. The authors are grateful to Mr. Julien Hunel for assistance with the SPM instrumentation.


## AUTHOR CONTRIBUTIONS

MPUH performed the experiments, JX fabricated efficient devices and MKN supervised the work, SK made electro-optical characterization and supervised MPUH, ZM, TB, LH, and DM performed and analyzed the spectroscopic experiments, and LH, DM supervised the work. SA drafted the first version and directed the work, and all authors commented and approved the final version of the manuscript.

## DECLARATION OF INTERESTS

The authors declare no competing interests.

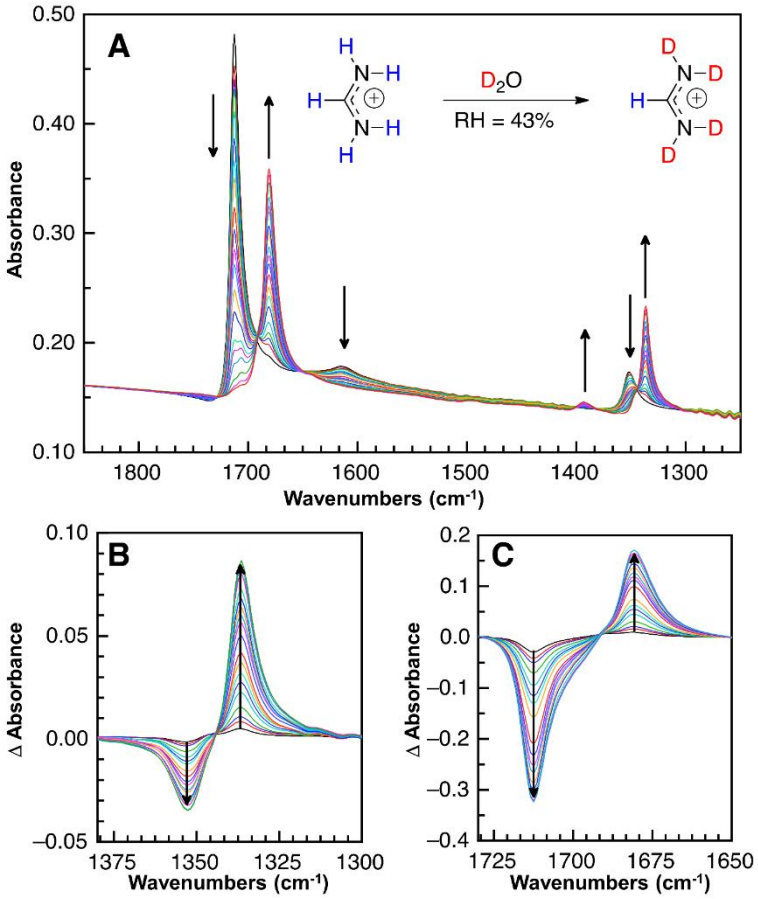


**Figure 1. Spectral variation during the H / D exchange**

(A) Evolution of the transmission IR spectra of a film (200µm thick) prepared from α-$FAPbI_3$ exposed to 43% RH $D_2O$ ($t$ = 0 to 100 h) and (B and C) Zoom of differential absorption spectra ($Abs_t - Abs_{t=0}$). The presence of isosbestic points is visible in both the absolute (top) and differential (bottom) absorption spectra.

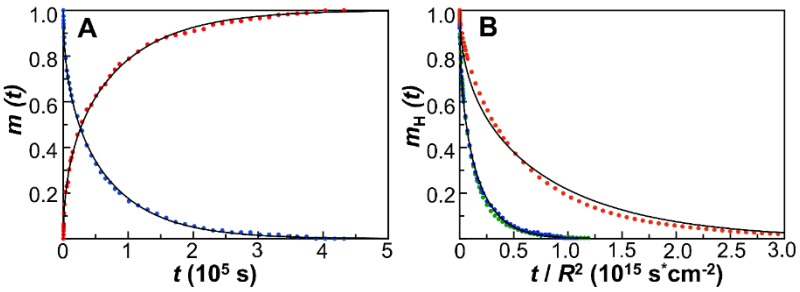


**Figure 2. Relative H/D composition**

(A) Relative hydrogen (blue symbols) and deuterium (red symbols) composition of thin films of $FAPbI_3$ exposed to $D_2O$ (RH = 43%) at room temperature determined from vibrations assigned to pure N–H or N–D modes. Solid black lines are the best fit for eq(1), (B) Comparison of the proportion of hydrogen present in thin films prepared from $FAPbI_3$ from α-powder (blue symbols), $FAPbI_3$ from δ-powder (green symbols), and $CsFAPbI_3$ (red symbols), as determined from the sum of the vibrations at 1712 $cm^{-1}$ and 1352 $cm^{-1}$, exposed to $D_2O$ (RH = 43%) at room temperature. Solid black lines are the best fit for eq(1).

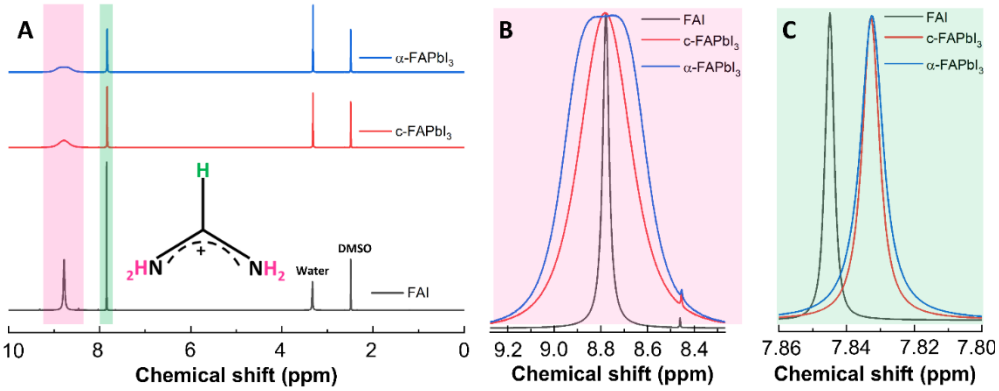


**Figure 3. $^{1}$H-NMR characterization of precursor solutions**

(A) Solution $^{1}$H-NMR spectra of FAI, conventional-$FAPbI_3$ and α-$FAPbI_3$ in DMSO-$D_6$ solvent at 25°C , the FA cation structure has been given in the inset; (B and C) Zoom-in view of Solution $^{1}$H-NMR spectra of, (B) –$NH_2$ protons and, (C) –CH protons in all the three solutions.

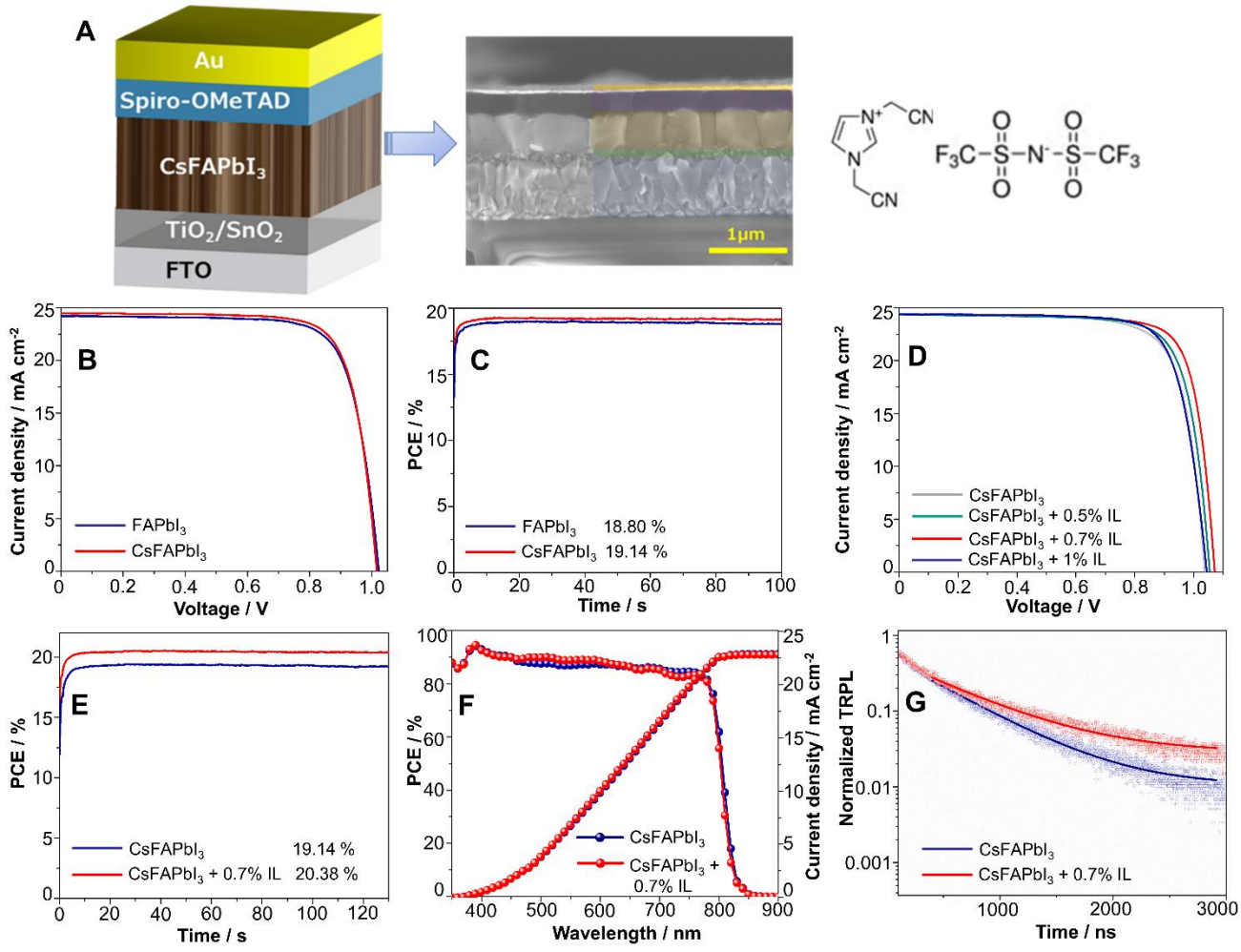


**Figure 4. Scheme, and electro-optical analysis of perovskites and solar cells**

(A) Schematic diagram and the corresponding cross-section image of $CsFAPbI_3$ based solar cells, the molecular structure of ionic liquids used, (B) *J-V* curves of devices based on $FAPbI_3$ and $CsFAPbI_3$, (C) the steady-state PCE of PSCs based on $FAPbI_3$ and $CsFAPbI_3$, (D) The champion *J-V* curves of $CsFAPbI_3$ based PSC doped with the various concentrations of IL, (E) the steady-state PCE of PSCs based on pristine $CsFAPbI_3$ and doped with 0.7 mol% IL, (F) IPCE of the devices based on $CsFAPbI_3$ (22.86 mA $cm^{-2}$) and doped with 0.7 mol% IL (22.81 mA $cm^{-2}$), (G) PL decay curve of pristine $CsFAPbI_3$ and 0.7 mol% IL doped $CsFAPbI_3$ perovskite film deposited on glass.

**Table1. Diffusion constants for protons (H) in pristine perovskite**

| Material | *R* (nm) | *D* ($cm^2\ s^{-1}$)[a] |
|---|---|---|
| $FAPbI_3$ from α-powder | 200 | $5.1 \times 10^{-16}$ |
| $FAPbI_3$ from δ-powder | 200 | $5.2 \times 10^{-16}$ |
| $CsFAPbI_3$ from α-powder | 140 | $1.1 \times 10^{-16}$ |

[a]Determined using eq(1) according to the average grain size *R* obtained from AFM and SEM analysis of the samples.

**Table 2. Photovoltaic parameters of the devices based on pristine $FAPbI_3$, $CsFAPbI_3$, and IL doped $CsFAPbI_3$ based solar cells.**

| **Perovskites** | | **$J_{SC}$ (mA $cm^{-2}$)** | **$V_{OC}$ (mV)** | **FF (%)** | **PCE (%)** |
|---|---|---|---|---|---|
| **$FAPbI_3$** | Max | 24.22 | 1022 | 76.2 | 18.85 |
| | Average | 23.51±0.71 | 993±29 | 74.5±1.7 | 17.40±1.45 |
| **$CsFAPbI_3$** | Max | 24.38 | 1036 | 76.3 | 19.27 |
| | Average | 23.78±0.6 | 1011±25 | 74.4±1.9 | 17.90±1.37 |
| **$CsFAPbI_3$+IL 0.5 %** | Max | 24.36 | 1054 | 77.2 | 19.82 |
| | Average | 23.80±0.56 | 1004±50 | 75.2±2 | 18.00±1.82 |
| **$CsFAPbI_3$+ IL 0.7 %** | Max | 24.36 | 1072 | 78.7 | 20.55 |
| | Average | 23.43±0.93 | 1036±36 | 76.9±2.1 | 18.63±1.92 |
| **$CsFAPbI_3$+ IL 1 %** | Max | 24.40 | 1043 | 76.8 | 19.54 |
| | Average | 23.78±0.62 | 1015±28 | 75.7±1.1 | 18.16±1.38 |

**Table 3. Fitting parameters of *mono*-exponential decay function in TRPL measurements of $CsFAPbI_3$ perovskite in pristine form and with 0.7 mol% IL doping.**

| Film | $\tau$ (ns) |
|---|---|
| Glass/$CsFAPbI_3$ | 516.1 |
| Glass/ $CsFAPbI_3$+ 0.7 % | 614 |

**REFERENCES**


(1) Kim, H.-S., Lee, C.-R., Im, J.-H., Lee, K.-B., Moehl, T., Marchioro, A., Moon, S.-J., Humphry-Baker, R., Yum, J.-H., Moser, J.E., et al. (2012). Lead Iodide Perovskite Sensitized All-Solid-State Submicron Thin Film Mesoscopic Solar Cell with Efficiency Exceeding 9%. Sci. Rep. *2*, 591. https://doi.org/10.1038/srep00591.

(2) Pellet, N., Gao, P., Gregori, G., Yang, T.-Y., Nazeeruddin, M.K., Maier, J., and Grätzel, M. (2014). Mixed-Organic-Cation Perovskite Photovoltaics for Enhanced Solar-Light Harvesting. Angew. Chem. Int. Ed. *53*, 3151–3157. https://doi.org/10.1002/anie.201309361.

(3) Koh, T.M., Fu, K., Fang, Y., Chen, S., Sum, T.C., Mathews, N., Mhaisalkar, S.G., Boix, P.P., and Baikie, T. (2013). Formamidinium-Containing Metal-Halide: An Alternative Material for Near-IR Absorption Perovskite Solar Cells. J. Phys. Chem. C *118* (30). 16458–16462. https://doi.org/10.1021/jp411112k.

(4) Juarez-Perez, E.J., Ono, L.K., Uriarte, I., Cocinero, E.J., and Qi, Y. (2019). Degradation Mechanism and Relative Stability of Methylammonium Halide Based Perovskites Analyzed on the Basis of Acid–Base Theory. ACS Appl. Mater. Interfaces *11* (13). 12586–12593. https://doi.org/10.1021/acsami.9b02374.

(5) Zheng, C., and Rubel, O. (2019). Unraveling the Water Degradation Mechanism of $CH_3NH_3PbI_3$. J. Phys. Chem. C *123* (32). 19385–19394. https://doi.org/10.1021/acs.jpcc.9b05516.

(6) Ceratti, D.R., Cohen, A.V., Tenne, R., Rakita, Y., Snarski, L., Jasti, N.P., Cremonesi, L., Cohen, R., Weitman, M., Rosenhek-Goldian, I., et al. (2021). The pursuit of stability in halide perovskites: the monovalent cation and the key for surface and bulk self-healing. Mater. Horiz. *8*, 1570–1586. doi:10.1039/d1mh00006c.

(7) Binek, A., Hanusch, F.C., Docampo, P., and Bein, T. (2015). Stabilization of the Trigonal High-Temperature Phase of Formamidinium Lead Iodide. J. Phys. Chem. Lett. *6*, 1249–1253. doi:10.1021/acs.jpclett.5b00380.

(8) Moloney, E.G., Yeddu, V., and Saidaminov, M.I. (2020). Strain Engineering in Halide Perovskites. ACS Mater. Lett. *2*, 1495–1508. doi:10.1021/acsmaterialslett.0c00308.

(9) Jena, A.K., Kulkarni, A., and Miyasaka, T. (2019). Halide Perovskite Photovoltaics: Background, Status, and Future Prospects. Chem. Rev. 119(5), 3036–3103. doi:10.1021/acs.chemrev.8b00539.

(10) Wang, S., Tan, L., Zhou, J., Li, M., Zhao, X., Li, H., Tress, W., Ding, L., Graetzel, M., and Yi C. (2022). Over 24% efficient MA-free CsxFA1−xPbX3 perovskite solar cells. Joule *6* (6), 1344–1356. doi:10.1016/j.joule.2022.05.002.

(11) Liu, S., Guan, Y., Sheng, Y., Hu, Y., Rong, Y., Mei, A., and Han, H. (2019). A Review on Additives for Halide Perovskite Solar Cells. Adv. Energy Mater. *10*, 1902492. doi:10.1002/aenm.201902492.

(12) Kim, E.-B., Akhtar, M.S., Shin, H.-S., Ameen, S., and Nazeeruddin, M.K. (2021). A review on two-dimensional (2D) and 2D-3D multidimensional perovskite solar cells: Perovskites structures, stability, and photovoltaic performances. J. Photochem. Photobiol. C: Photochem. Rev. *48*, 100405. https://doi.org/10.1016/j.jphotochemrev.2021.100405.

(13) Kim, J., Ho‐Baillie, A., and Huang, S. (2019). Review of Novel Passivation Techniques for Efficient and Stable Perovskite Solar Cells. Sol. RRL *3*, 1800302. https://doi.org/10.1002/solr.201800302.

(14) Haris, M.P.U., Kazim, S., and Ahmad, S. (2021). Low-Temperature-Processed Perovskite Solar Cells Fabricated from Presynthesized $CsFAPbI_3$ Powder. ACS Appl. Energy Mater. *4*, 2600–2606. https://doi.org/10.1021/acsaem.0c03160.

(15) Sánchez, S., Cacovich, S., Vidon, G., Guillemoles, J.-F., Eickemeyer, F., Zakeeruddin, S.M., Schawe, J.E.K., Löffler, J.F., Cayron, C., Schouwink, P., et al. (2022). Thermally controlled growth of photoactive $FAPbI_3$ films for highly stable perovskite solar cells. Energy Environ. Sci. *15*, 3862–3876. https://doi.org/10.1039/D2EE01196D.

(16) Li, H., Zhou, J., Tan, L., Li, M., Jiang, C., Wang, S., Zhao, X., Liu, Y., Zhang, Y., Ye, Y., et al. (2022). Sequential vacuum-evaporated perovskite solar cells with more than 24% efficiency. Science Advances *8*, eabo7422. https://doi.org/10.1126/sciadv.abo742.

(17) Doherty, T.A.S., Nagane, S., Kubicki, D.J., Jung, Y.-K., Johnstone, D.N., Iqbal, A.N., Guo, D., Frohna, K., Danaie, M., Tennyson, E.M., et al. (2021). Stabilized tilted-octahedra halide perovskites inhibit local formation of performance-limiting phases. Science *374*, 1598–1605. https://doi.org/10.1126/science.abl4890.

(18) Kim, G., Min, H., Lee, K.S., Lee, D.Y., Yoon, S.M., and Seok, S.I. (2020). Impact of strain relaxation on performance of α-formamidinium lead iodide perovskite solar cells. Science *370*, 108–112. https://doi.org/10.1126/science.abc4417.

(19) Boyd, C.C., Cheacharoen, R., Leijtens, T., and McGehee, M.D. (2018). Understanding Degradation Mechanisms and Improving Stability of Perovskite Photovoltaics. Chem. Rev. *119*, 3418–3451. https://doi.org/10.1021/acs.chemrev.8b00336.

(20) Holzhey, P., and Saliba, M. (2018). A full overview of international standards assessing the long-term stability of perovskite solar cells. J. Mater. Chem. A. *6*, 21794–21808. https://doi.org/10.1039/C8TA06950F.

(21) Haris, M.P.U., Kazim, S., Pegu, M., Deepa, M., and Ahmad, S. (2021). Substance and shadow of formamidinium lead triiodide based solar cells. Phys. Chem. Chem. Phys. *23*, 9049–9060. https://doi.org/10.1039/D1CP00552A.

(22) Zhang, D., Li, D., Hu, Y., Mei, A., and Han, H. (2022). Degradation pathways in perovskite solar cells and how to meet international standards. Commun. Mater. *3*, 58. https://doi.org/10.1038/s43246-022-00281-z.

(23) Ho, K., Wei, M., Sargent, E.H., and Walker, G.C. (2021). Grain Transformation and Degradation Mechanism of Formamidinium and Cesium Lead Iodide Perovskite under Humidity and Light. ACS Energy Lett. *6*, 934–940. https://doi.org/10.1021/acsenergylett.0c02247.

(24) Walsh, A., and Stranks, S.D. (2018). Taking Control of Ion Transport in Halide Perovskite Solar Cells. ACS Energy Lett. *3*, 1983–1990. https://doi.org/10.1021/acsenergylett.8b00764.

(25) Yang, B., Brown, C.C., Huang, J., Collins, L., Sang, X., Unocic, R.R., Jesse, S., Kalinin, S.V., Belianinov, A., Jakowski, J., et al. (2017). Enhancing Ion Migration in Grain Boundaries of Hybrid Organic–Inorganic Perovskites by Chlorine. Adv. Funct. Mater. *27*, 1700749. https://doi.org/10.1002/adfm.201700749.

(26) Harvey, S.P., Li, Z., Christians, J.A., Zhu, K., Luther, J.M., and Berry, J.J. (2018). Probing Perovskite Inhomogeneity beyond the Surface: TOF-SIMS Analysis of Halide Perovskite Photovoltaic Devices. ACS. Appl. Mater. Interfaces *10*, 28541–28552. https://doi.org/10.1021/acsami.8b07937.

(27) Braun, A., and Chen, Q. (2017). Experimental neutron scattering evidence for proton polaron in hydrated metal oxide proton conductors. Nat. Commun. *8*, 15830. https://doi.org/10.1038/ncomms15830.

(28) Sadhu, S., Buffeteau, T., Sandrez, S., Hirsch, L., and Bassani, D.M. (2020). Observing the Migration of Hydrogen Species in Hybrid Perovskite Materials through D/H Isotope Exchange. J. Am. Chem. Soc. *142* (23), 10431–10437. https://doi.org/10.1021/jacs.0c02597.

(29) Ceratti, D.R., Zohar, A., Kozlov, R., Dong, H., Uraltsev, G., Girshevitz, O., Pinkas, I., Avram, L., Hodes, G., and Cahen, D. (2020). Eppur si Muove: Proton Diffusion in Halide Perovskite Single Crystals. Adv. Mater. *32*, 2002467. https://doi.org/10.1002/adma.202002467.

(30) Zhang, Y., Kim, S.-G., Lee, D.-K., and Park, N.-G. (2018). CH3 NH3 PbI3 and HC(NH2 )2 PbI3 Powders Synthesized from Low-Grade PbI2 : Single Precursor for High-Efficiency Perovskite Solar Cells. ChemSusChem *11*, 1813–1823. https://doi.org/10.1002/cssc.201800610.

(31) Jeong, J., Kim, M., Seo, J., Lu, H., Ahlawat, P., Mishra, A., Yang, Y., Hope, M.A., Eickemeyer, F.T., Kim, M., et al. (2021). Pseudo-halide anion engineering for α-FAPbI 3 perovskite solar cells. Nature *592*, 381–385. https://doi.org/10.1038/s41586-021-03406-5.

(32) Haris, M.P.U., Kazim, S., and Ahmad, S. (2022). Microstrain and Urbach Energy Relaxation in $FAPbI_3$-Based Solar Cells through Powder Engineering and Perfluoroalkyl Phosphate Ionic Liquid Additives. ACS Appl. Mater. Interfaces *14* (21), 24546–24556. https://doi.org/10.1021/acsami.2c01960.

(33) Kucharska, E., Hanuza, J., Ciupa, A., Mączka, M., and Macalik, L. (2014). Vibrational properties and DFT calculations of formamidine-templated Co and Fe formates. Vib. Spectrosc. *75*, 45-50. https://doi.org/10.1016/j.vibspec.2014.09.001.

(34) Buffeteau, T., Hirsch, L., and Bassani, D.M. (2021). Comment on "Eppur si Muove: Proton Diffusion in Halide Perovskite Single Crystals": Eppur Non si Muove: A Critical Evaluation of Proton Diffusion in Halide Perovskite Single Crystals. Adv. Mater. *33*, 2007715. https://doi.org/10.1002/adma.202007715.

(35) Jung, M., Ji, S.-G., Kim, G., and Seok, S.I. (2019). Perovskite precursor solution chemistry: from fundamentals to photovoltaic applications. Chem. Soc. Rev. *48*, 2011—2038. https://doi.org/10.1039/C8CS00656C.

(36) Lee, J.-W., Kim, D.-H., Kim, H.-S., Seo, S.-W., Cho, S.M., and Park, N.-G. (2015). Formamidinium and Cesium Hybridization for Photo- and Moisture-Stable Perovskite Solar Cell. *Adv. Energy. Mater. 5* (20). https://doi.org/10.1002/aenm.201501310.

(37) Salado, M., Kazim, S., and Ahmad, S. (2018). The role of Cs+ inclusion in formamidinium lead triiodide-based perovskite solar cell. Chem. Pap. *72*, 1645–1650. https://doi.org/10.1007/s11696-017-0373-7.

(38) Gao, X.-X., Ding, B., Kanda, H., Fei, Z., Luo, W., Zhang, Y., Shibayama, N., Züttel, A., Tirani, F.F., Scopelliti, R., et al. (2021). Engineering long-term stability into perovskite solar cells via application of a multi-functional TFSI-based ionic liquid. Cell Rep. Phys. Sci. *2* (7), 100475. https://doi.org/10.1016/j.xcrp.2021.100475.

(39) Wang, S., Li, Z., Zhang, Y., Liu, X., Han, J., Li, X., Liu, Z., Frank) Liu, S., and Choy, W.C.H. (2019). Water‐Soluble Triazolium Ionic‐Liquid‐Induced Surface Self‐Assembly to Enhance the Stability and Efficiency of Perovskite Solar Cells. Adv. Funct. Mater. *29*, 1900417. https://doi.org/10.1002/adfm.201900417.

(40) Wang, Y., Yang, Y., Li, N., Hu, M., Raga, S.R., Jiang, Y., Wang, C., Zhang, X., Lira‐Cantu, M., Huang, F., et al. (2022). Ionic Liquid Stabilized Perovskite Solar Modules with Power Conversion Efficiency Exceeding 20%. Adv. Funct. Mater. *32*, 2204396. https://doi.org/10.1002/adfm.202204396.

(41) Stolterfoht, M., Wolff, C.M., Márquez, J.A., Zhang, S., Hages, C.J., Rothhardt, D., Albrecht, S., Burn, P.L., Meredith, P., Unold, T., et al. (2018). Visualization and suppression of interfacial recombination for high-efficiency large-area pin perovskite solar cells. Nat. Energy *3*, 847–854. https://doi.org/10.1038/s41560-018-0219-8.